GEOLOGY

The magmatic origin of the Columbia River Gorge, USA

Nathaniel Klema[1,2]*, Leif Karlstrom[1], Charles Cannon[3], Chengxin Jiang[4], Jim O'Connor[3], Ray Wells[3], Brandon Schmandt[5]

Along subduction zones, high-relief topography is associated with sustained volcanism parallel to the plate margin. However, the relationship between magmatism and mountain building in arcs is poorly understood. Here, we study patterns of surface deformation and correlated fluvial knickpoints in the Columbia River Gorge to link long-term magmatism to the uplift and ensuing topographic development of the Cascade Range. An upwarped paleochannel exposed in the walls of the Gorge constrains unsteady deep magma flux, the ratio of intrusive to extrusive magmatic contributions to topography, and the impact of magmatism on Columbia River incision since 3.5 million years ago. Geophysical data indicate that deep magma influx beneath the arc axis is ongoing and not aligned with the current locations of volcanic edifices, representing a broad regional influence on arc construction.

INTRODUCTION

Volcanic arcs represent the highest, steepest, and the most rapidly changing topography at subduction zones. Localized and unsteady uplift driven by magmatism, superimposed on background tectonic deformation, makes these terrains an outstanding laboratory for the study of volcanic mountain building (*1*, *2*). For more than 100 years, the Columbia River Gorge (hereafter the Gorge), an enigmatic high-relief landscape that has shaped human society in the region (*3*, *4*), has been recognized as a natural laboratory for arc processes (*5*). As the largest river on Earth to cross an active volcanic arc, the Columbia River has dissected the Cascades for at least 17 million years (Ma) (*6*), exposing a cross section of the Cascade Range and serving as a near-sea-level base level driving erosion of the surrounding landscape.

As the regional topographic low, the Columbia River corridor has received, conveyed, and been diverted by lava flows from Columbia River Flood Basalt volcanism to the east and locally from the Cascade volcanic arc that it bisects (*7*). Remnants of these volcanic deposits record subsequent deformation of the arc by their position relative to the modern Columbia River (*8*). An especially prominent structural datum is marked by the most recent Columbia River diversion in the Gorge at 3.5 to 3.0 Ma ago, when arc-derived lava flows and associated hyaloclastite filled the existing valley and displaced the river northward to its modern course (*9*). Hyaloclastite deposits filling this "Bridal Veil" (BV) paleochannel (Fig. 1) record a subsequent ~900 m of asymmetric anticlinal uplift spanning ~80 km of the arc (*9*). A superposition of this uplift and overlying erupted deposits forms the iconic high-relief topography of the Gorge, which locally rises to 1512 m at the shield volcano Mount Defiance.

Clockwise rotation of the forearc relative to North America (Fig. 1) since at least the early Miocene (*10*) provides a framework to analyze the underlying drivers of this uplift. North of the Columbia River, tectonic rotation produces compression, mainly manifest by east-west–oriented folds and thrust faults (*7*). South of the Columbia River, the regime is mostly extensional as evidenced by north-south–oriented normal faults. Rotational shear is accommodated by right lateral displacements on north to north-northwest trending strike-slip faults (*11*, *12*). The Columbia River thus sits at a transition point where tectonic strain is dominantly north-south, making crustal shortening an unlikely source of the broad east-west uplift centered on the Gorge. Instead, we hypothesize that the uplift is due primarily to magmatic crustal inflation. We will show that late Pliocene and Quaternary deformation of BV channel deposits is a flexural response to magmatic intrusions below an elastic upper crust. Magmatic forcing is active at present, as inferred from gravity, heat flow, and seismic tomography coincident with uplift, and patterns of Quaternary volcanism. Current Columbia tributary drainages record transient topographic adjustment to this spatially variable magmatic uplift field in the form of fluvial knickpoints that mirror uplift of the BV paleochannel (Fig. 1B).

RESULTS

Transcrustal magmatic structure

The mechanical response of Earth's crust to an applied load depends on the magnitude and spatial wavelengths of forcing as well as rheological properties that are strongly time and temperature dependent (*13*, *14*). If the crust is approximated as a thin elastic plate of uniform thickness, then the lateral wavelength of deformation is set by a flexural rigidity that scales with effective elastic plate thickness (T_e) cubed (*15*). In arcs, heat released from generations of magmatic intrusions ascending through a transcrustal transport network (*16*) promotes shallowing of T_e through time as crustal heating promotes a ductile mechanical response at depth (*17*). Intrusions dilate overlying elastic crust, producing a mechanical response that approximates a thin elastic plate with T_e set by this rheologic transition (*18*, *19*). This model, although it neglects contributions from spatially heterogeneous plate properties, is sufficient to address available constraints relating long-term Gorge magmatism to the evolution of the upper crust.

The magnitude and pattern of uplift recorded in BV channel hyaloclastites is well modeled with T_e = 4- to 11-km subject to a net

[1]Department of Earth Sciences, University of Oregon, Eugene, OR, USA. [2]Department of Physics and Engineering, Fort Lewis College, Durango, CO, USA. [3]U.S. Geological Survey, Portland, OR, USA. [4]Research School of Earth Sciences, The Australian National University, Acton, ACT, Australia. [5]Department of Earth and Planetary Sciences, University of New Mexico, Albuquerque, NM, USA.
*Corresponding author. Email: ntklema@fortlewis.edu

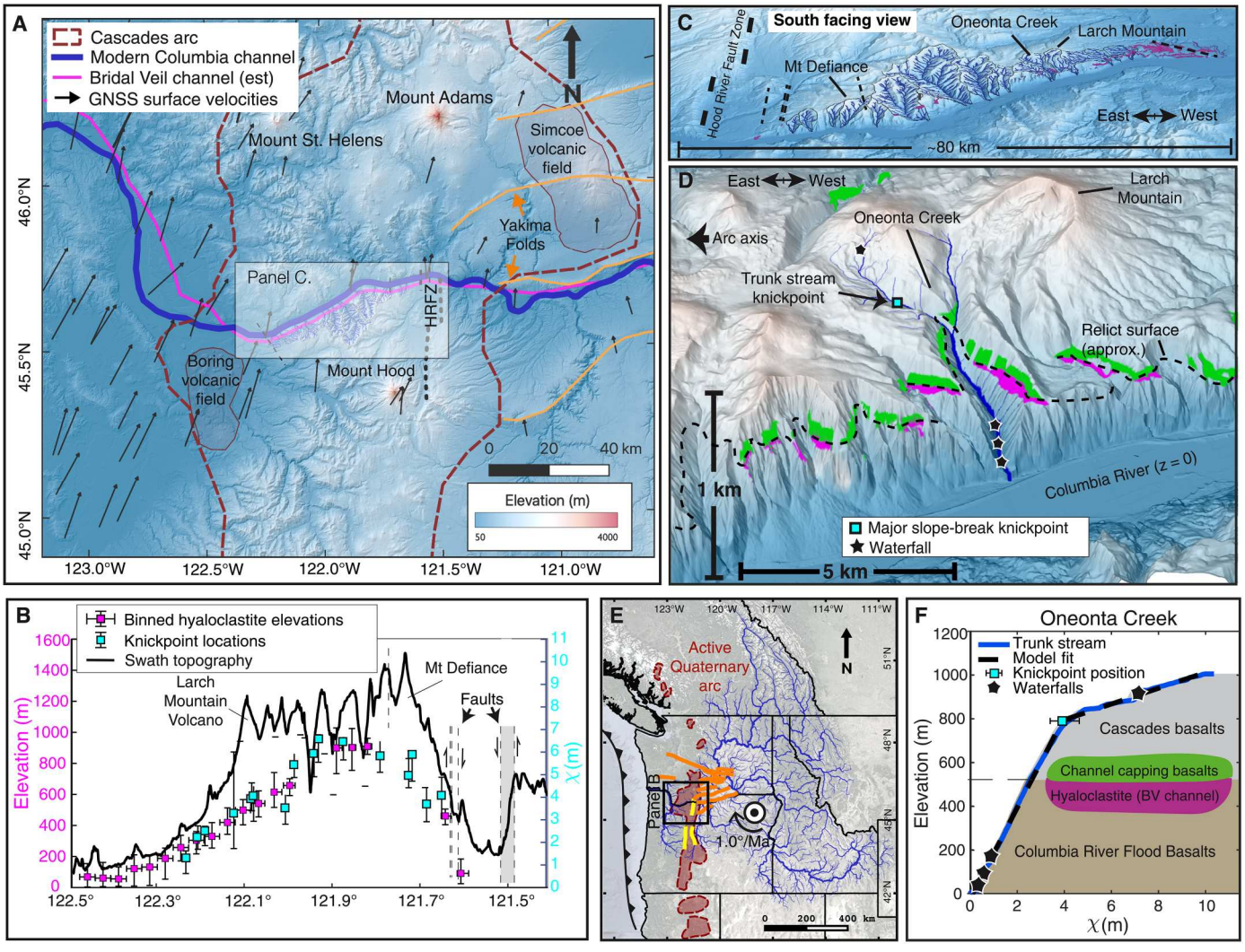

Fig. 1. Overview of the Columbia River Gorge. (**A**) Structural setting, showing GNSS velocities with respect to stable North American reference frame (*52*) (black arrows), Yakima Folds (orange lines), the modern and paleo Bridal Veil (BV) Columbia River channels (blue and pink lines), and extent of the Cascades arc (red dash lines). HRFZ, Hood River Fault Zone. (**B**) BV hyaloclastite deposits and best-fitting knickpoint locations in Columbia River tributaries. Maximum topographic elevations within 10 km south of the Columbia River (black line) with prominent faults (dashed lines) (*57*). (**C**) Southward orthoview of fluvial catchments, hyaloclastite deposits, and major faults. (**D**) Southward orthoview of Oneonta Creek showing the trunk stream knickpoint used in this study (large blue square), and waterfalls associated with layered basalt stratigraphy (black stars). (**E**) Regional map of the Columbia River drainage network, showing the Euler pole for Cascadia forearc block relative to North America (*10*). Orange lines are compressional structures while yellow lines mark arc-marginal normal faults. (**F**) Longitudinal profile using area-normalized upstream distance χ(*x*) for Oneonta Creek with best fitting slope-break knickpoint (section S2).

upward force of ~34×10^6 N distributed over a wavelength of 110 to 130 km. Removal of crust via erosion by the Columbia River and its tributaries contributes to this force imbalance, but not enough for isostatic rebound to be a primary driver of uplift. We estimate the removal of 270 km^3 of sediment by erosion in tributaries of the Columbia that enter within the Gorge. For values of T_e that fit the deformation wavelength of hyaloclastite erosion could contribute ~120 m of flexural uplift at most (section S7). However, this unloading is offset by a similar volume of erupted material deposited on top of the paleosurface by Cascade Range volcanoes. We therefore neglect erosional unloading relative to magmatic inflation in forcing hyaloclastite uplift. This amount of bedrock uplift and resultant exhumation by Columbia River incision are similar to values in major tectonic orogens (*20*); however, these situations may not be directly comparable to the Gorge due to complications of magmatic forcing and the attenuation of loads in the flexural regime (sections S5 and S6).

Inference of intrusive magmatic forcing as a mechanism for bedrock uplift is augmented by a broad suite of indirect observations. Bouguer gravity data (*21*), although not corrected for locally steep topography or laterally heterogeneous subsurface structures, show a negative anomaly over the arc consistent with flexural uplift due to a buried load (section S4 and fig. S6). Similarly, regionally interpolated heat flow (*22*) has a local maximum over the arc and implies a long-lived magmatic heat source. Both datasets are consistent with elevated temperatures and silicate melt under the

area of maximum hyaloclastite uplift at present and likely since the onset of hyaloclastite deformation (Fig. 2).

High-resolution seismic tomography using Rayleigh and Love waves (*23*) shows a region of low shear-wave velocities (V_S) at depths >20 km beneath the arc with magnitudes that likely require both partial melt and elevated temperatures (section S8). The seismic anomaly is aligned with hyaloclastite deformation in the Gorge and extends northwest and southeast connecting Mount St. Helens and Mount Hood at 20- to 30-km depth (Fig. 2) (*23*).

Long-term balance of intrusions versus eruptions

Regional covariance along the Cascade Range between crustal geophysical anomalies and high topography associated with Quaternary volcanic vents (*24*) suggests that magmatism contributes to uplift throughout the arc. However, understanding the partitioning between intrusive and extrusive (i.e., eruptions) modes of magmatism is challenging (*25*), so the rates of topographic growth from intrusive magmatic processes are difficult to quantify. The cross section of the Cascade Range created by the Columbia River provides an opportunity to estimate the ratio of intrusive to extrusive magmatism (I:E) on million-year timescales and assess the relative contribution of each to arc mountain building.

A lower bound estimate for the volume of intruded magma can be calculated as the amount of accommodation space created by hyaloclastite deflection between the western margin of uplift and the fault-bounded eastern margin of uplift (Figs. 3 and 1B). Because all material overlying the hyaloclastite originated in the Cascades, the total extruded volcanic output can be estimated as the difference in elevation between this paleosurface and modern topography. If we assume an onset time between 3.5 and 3.0 Ma ago (section S1), then this gives average intrusive and extrusive magma flux estimates of 10 to 13 km^3/Ma per kilometer and 3 to 4 km^3/Ma per kilometer, respectively. Accounting for spatially variable topography within a 10-km swath south of the Columbia River (assuming that intrusive uplift is unchanged) gives a distribution with 95% confidence interval of I:E = $2.9^{+3.6}_{-2.4}$ (Fig. 3).

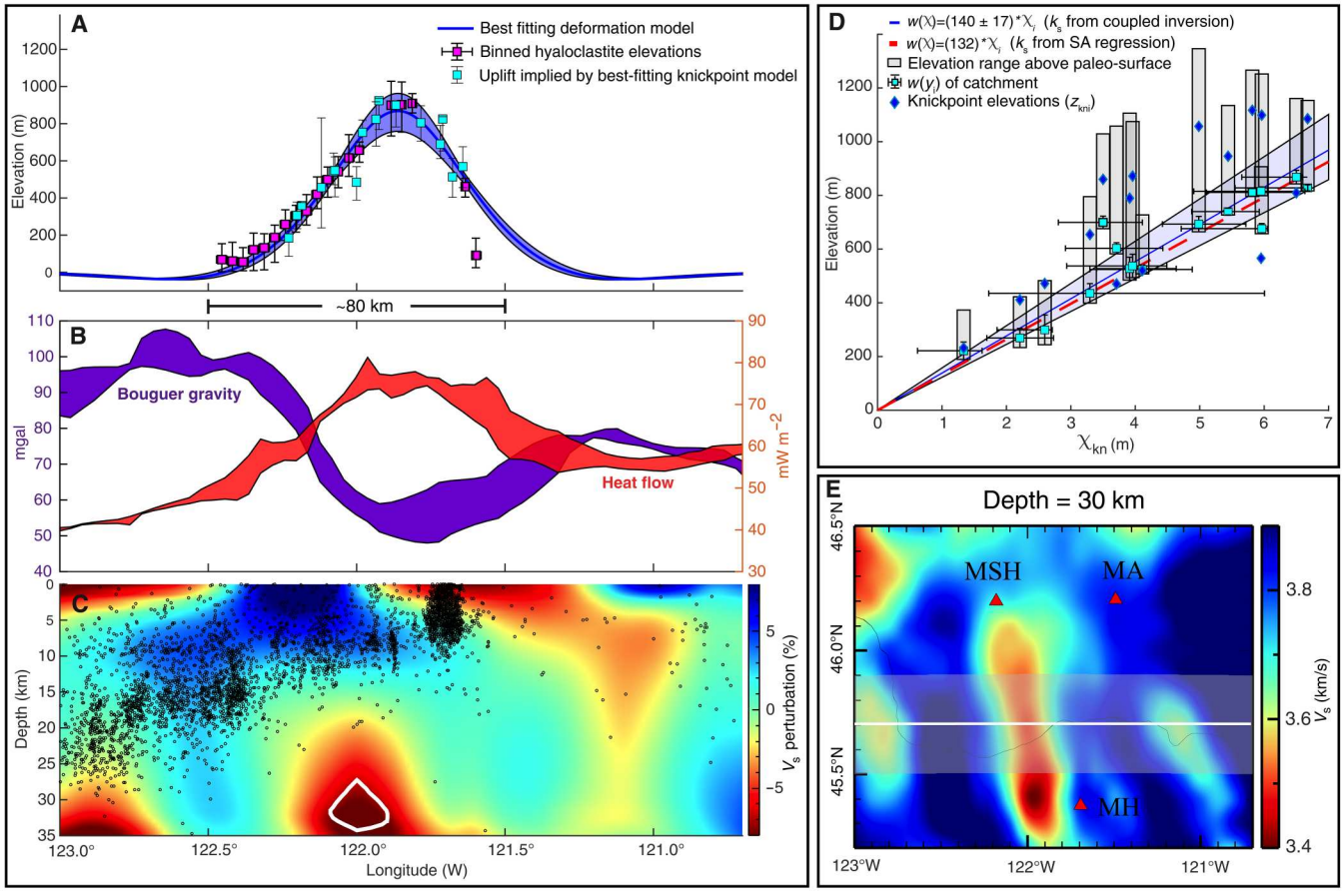

Fig. 2. Geophysical anomalies across the Gorge and their relationships to deformation of the BV paleochannel. (**A**) Best-fitting uplift model from maximum likelihood estimation with 95% confidence model envelope. Light blue squares show knickpoint elevations inferred from a transient fluvial incision model forced by flexural uplift constrained by hyaloclastite deformation (pink squares). (**B**) Interpolated Bouguer gravity anomaly and surface heat flow. (**C**) Average shear-wave velocity anomaly. The white contour marks region of inferred 2.5 to 4% partial melt (section S8). Black dots are earthquake hypocenters underlying the Gorge since 1970 (*58*). (**D**) Hyaloclastite elevation (squares) and knickpoint elevation (diamonds) versus knickpoint location $\chi(x)_i$. Red dashed line shows uplift predicted by fluvial model using slope-area regression, while shaded swath shows model predictions (sections S2 and S5). Mismatch between $\chi(x)_i$ and knickpoint elevations likely implies time-evolving hydraulic conductivity/erodibility of young lava flows. (**E**) Regional map of shear-wave seismic velocity at 30-km depth showing swath in (C). Red triangles mark the volcanoes Mount St. Helens (MSH), Mount Adams (MA), and Mount Hood (MH).

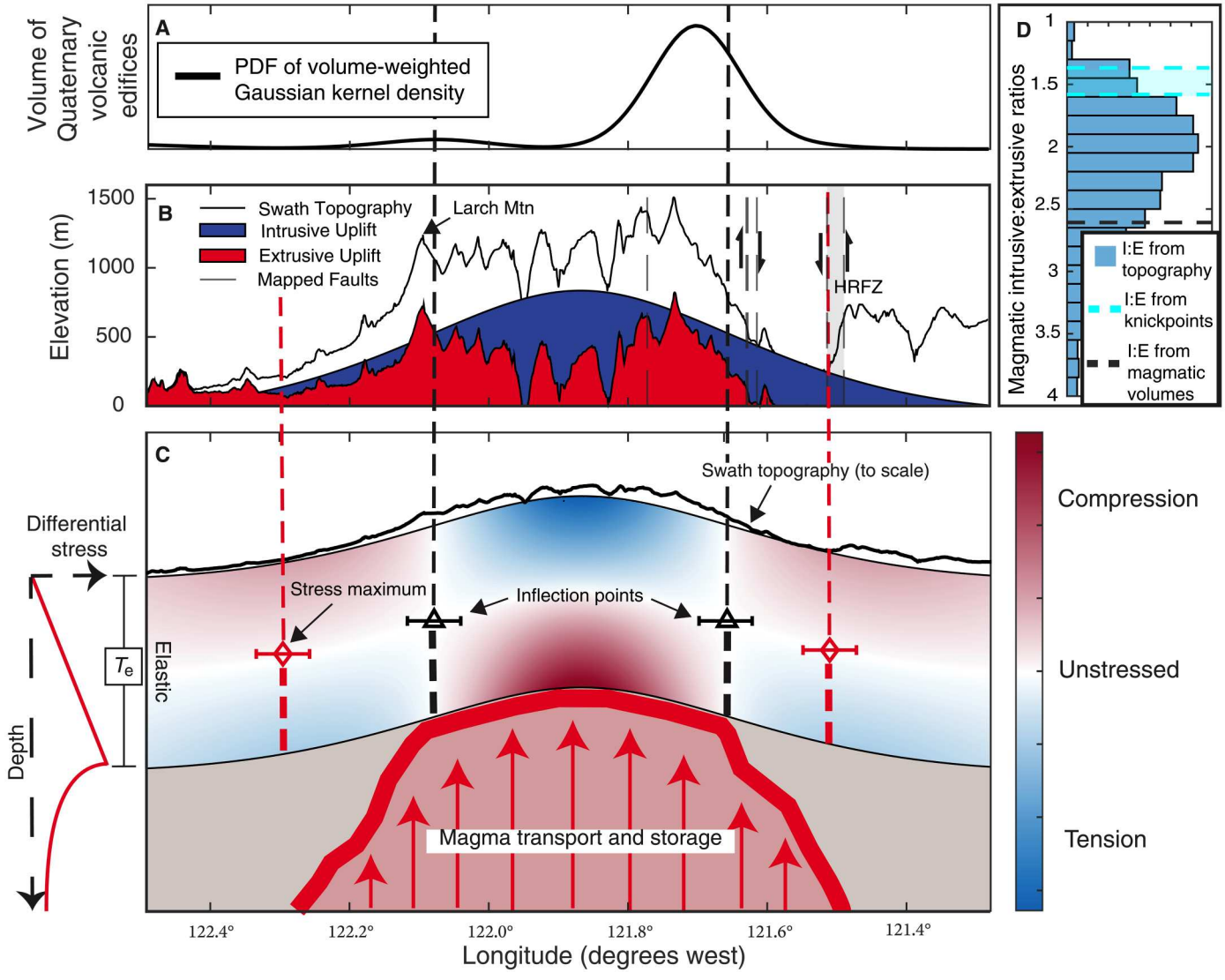

Fig. 3. Inference of transcrustal magmatic structure. (**A**) Volume-weighted Gaussian kernel density of Quaternary edifices within 10 km north and south of the Columbia (*24*). (**B**) Intrusive and extrusive magmatic topography, using best fitting flexural uplift model. Dashed lines indicate major fault systems that bound the Hood River Valley (*57*). (**C**) Best fitting plate model defining elastic thickness of the upper crust. Alternating tensile and compressional deviatoric stresses in the plate are inferred to direct shallow magma ascent and faulting. (**D**) Ratios of intrusive:extrusive (I:E) magmatism calculated using topography (assuming north-south continuity in flexural uplift), knickpoint positions, and total calculated volumes of erupted and intruded magma.

Our estimates are similar in magnitude to previous estimates of magmatic flux required to produce heat flow measured in the Cascades (*26*) of 9 to 33 km^3/Ma per kilometer. Together with eruptive flux estimates of 3 to 6 km^3/Ma per kilometer (*27*), this gives I:E = 1.5 to 11. Topographically derived I:E values for the Gorge are a lower bound, because they do not account for deep intrusions that generate longer wavelength deformation near the surface (*18*) and only account for magma underlying the deformed paleosurface. An upper bound on intrusive volume can be calculated by considering isostatic compensation to magmatic crustal thickening (*1*). Airy isostacy would require magmatic thickening of ~5.5 km and I:E ≈ 16 at the center of the arc. However, full isostatic compensation also implies unrealistically small values of effective elastic thickness (fig. S9), and so we do not favor this scenario.

Seismic tomography of present day crustal structure suggests ongoing intrusion and provides a modern context for these flux estimates. The volume of stored partial melt implied by seismic anomalies depends on lower crustal compositions, temperature, and grain boundary melt geometry (*28*). Petrologic constraints on storage temperatures for Mount St. Helens magmas suggest lower crustal temperatures in the range of 750° to 950°C (*29*). A long-lived magma storage zone in the lower crust with this temperature range is consistent with observed heat flow at the arc front (section S9). Assuming textural equilibrium of melt [energetically stable grain boundary geometries; (*28*, *30*)], seismic tomography suggests ~4-km^3 magma per kilometer of arc currently underneath the Cascade Range at this latitude.

Topographic response to magmatism

We can gain additional insight into temporal patterns of magmatism by leveraging the stable, near-sea-level base level imposed by the Columbia River as it transects the Cascade Range. Actively eroding landscapes tend toward dynamic equilibrium conditions wherein surface erosion and uplift are balanced and fluvial channels maintain power-law scaling between channel slope and upstream drainage area (*31*). An increase in uplift rate generates an upstream-propagating kinematic wave of incision that manifests as a step change in this relationship, referred to as a "slope-break knickpoint" (*32*). Thus, we expect that a past increase in the rate of magmatic uplift should be recorded in the slope-area relations of tributaries entering the Columbia River.

We focus on channels that enter from the south side of the Gorge where southward tilting bedrock limits deep-seated landsliding that is prevalent on the north side of the river (*33*) (section S2). Here, 16 prominent tributary streams entering the Columbia River provide a natural landscape evolution experiment in which adjacent streams are forced by a known uplift perturbation beginning at the same time (deposition of BV deposits) but with a magnitude that varies between tributaries. In all catchments, channels cut through similar layered basalt stratigraphy consisting of Cascades arc volcanic rock overlying Columbia River Flood Basalts and lenses of hyaloclastite (*9*). Variable basaltic layering causes sharp localized knickpoints in stream profiles (the iconic waterfalls of the Columbia Gorge); however, at the catchment scale, most tributaries contain a single slope-break knickpoint that separates each longitudinal profile into two segments with constant concavity but different slope-area scaling (Fig. 1).

The upstream position of these knickpoints tracks hyaloclastite deformation (Fig. 1), implicating a geomorphic adjustment to magmatic uplift. Knickpoint propagation speed depends on upstream drainage area (*A*) (*34*), and so to compare different sized catchments directly, we normalize upstream distance along each channel with respect to drainage area and examine knickpoint positions relative to the nondimensional upstream coordinate $\chi(x)$ (*35*). The "stream power" model for fluvial bedrock erosion in its simplest form predicts that a knickpoint associated with a step increase in uplift rate occurring at time τ_o will be located at position $\chi(x) = U\tau_o/k_s$ (section S2), where U is the average uplift rate and k_s is an empirical constant that scales the power law relationship between upstream drainage area and channel slope, $dz/dx = k_s A(x)^{-\theta}$ (*32*).

Flexural uplift requires continuity in the elastically deformed upper crust. In the region where the tributary catchments are located, this assumption is supported by a lack of major faulting (Fig. 1B). Mechanical coherence then requires that knickpoint onset time τ_o (coincident with diversion of the Columbia at 3.5 to 3.0 Ma) is the same for all catchments. A stream-power prediction for the relationship between knickpoint position $[\chi(x)_i]$ and bedrock uplift $[w(y_i)]$ can then be written as $w(y_i)/\chi(x)_i = k_s$ where $i = 1:16$ is a catchment index and y_i is the across-arc position of each tributary (fig. S3). This relationship maps hyaloclastite uplift onto knickpoint positions with $k_s = 140 \pm 17$ for all catchments (Fig. 2). This is similar to k_s values calculated in other rapidly uplifting landscapes (*36*, *37*), although we note that in general k_s is sensitive to differences in θ and this makes direct comparison difficult. In the Gorge, given the constraint of constant τ_o between channels, the correspondence between hyaloclastite uplift and knickpoint χ-location implies that knickpoint response times depend on relief and are not solely controlled by discharge as has been proposed elsewhere (*38*).

Inference of constant k_s across Gorge tributaries is consistent with fluvial erosion patterns in other high-relief landscapes. Although this parameter is sometimes assumed to covary with uplift rate (*32*), a global compilation of fluvial catchments in active tectonic settings (*37*) suggests an upper limit on k_s is set by threshold channel steepness in rapidly uplifting landscapes. Increase of coarse sediment supply with uplift, resulting in transport-limited conditions that modulate the efficiency of fluvial bedrock erosion (*39*), is one possible mechanism to achieve bounded k_s. However, it is also noteworthy that simple stream-power models are known to fall short of describing the full range of fluvial process regimes (*40*).

The upstream position of knickpoints is less well correlated to knickpoint elevations in channels (Fig. 2D), which instead reflect variations in the thickness of Pliocene-Quaternary arc lavas overlying the paleosurface (Fig. 3B). This observation is consistent with episodic deposition of volcanic bedrock, which leads to strong hydromechanical layering and hydraulic anisotropy that affects bedrock erosion long after primary emplacement (*41*). We conclude that young lava flows in the Gorge produce topographic relief but have negligible influence on time-averaged rates of channel incision in underlying strata.

The inferred relationship between knickpoint locations and hyaloclastite uplift shows that fluvial profiles record the relative contribution of intrusion versus eruption to topographic development. If the thickness of erupted deposits is the difference between observed channel elevations above the knickpoints (z_{kni}) and uplift associated with the knickpoints, then the ratio of intrusive to extrusive magmatic uplift can then be calculated directly from fluvial channels as $\text{I:E} = k_s\chi(x)_i/z_{kni} = 1.4 \pm 0.5$. The alignment of this lower bound with I:E calculated through other means (Fig. 3D) suggests that long-term magma dynamics can be encoded into river networks, as has been inferred for tectonic and/or climatic forcing in nonmagmatic landscapes (*36*).

DISCUSSION

Entwined upper crustal deformation, arc mountain building, and magma ascent

Broad, arc-centered crustal deformation in response to intrusive magmatism can explain several other primary features of the central Cascades arc. In particular, plate-like flexure of the elastic upper crust generates a combination of tensile and compressional stresses (*42*) that may explain prominent normal faults along the Hood River Fault Zone (Fig. 1). These extensional features are consistent with north-south maximum horizontal compressive stress and align with off-axis peaks in deviatoric stress from our best-fitting flexural model (Fig. 3). To the west of the arc front, subsidence of the Portland basin is coincident with the implied flexural bulge of our model (*43*). While flexure cannot itself explain the magnitude of subsidence there (or in the Hood River Valley to the east), the resulting topography would route fluvial sediments and erupted material to these arc margins to the east and west, causing further loading of the plate and increased subsidence (*44*).

Unusual spatial patterns of magmatism in the vicinity of the Columbia River, the widest point of the Quaternary Cascades arc (*45*), may also reflect the influence of shallow crustal stresses implied by

our model. Within the Gorge, local maxima in both the volume-weighted Gaussian kernel density of volcanic vents (*24*) and the thickness of associated erupted deposits are located east and west of the maximum hyaloclastite layer deformation (Fig. 3). This is consistent with compressional flexural stresses in the lower half of an elastic upper crust that route ascending magma toward off-axis minima in differential stresses (*42*). The most active Holocene Cascades volcano, Mount St. Helens, sits notably off-axis and in the forearc northwest of the Gorge. Arc-centered flexure can contribute to observed lateral migration of ascending magma around inherited upper crustal structures (*46*).

Outside the Gorge, local widening of the Quaternary arc is associated with the Boring and Simcoe distributed vent fields (Fig. 1) (*45*). The Columbia River itself could play a role in this local widening of arc magmatic surface expression, as surface unloading from persistent fluvial incision generates topographic stresses known to influence magma ascent pathways in other settings (*47*). Current topography represents a ~25-MPa topographic load difference between the Gorge and adjacent arc (*48*). Quaternary average erosion/sediment production rates implied by projecting the hyaloclastite layer over the Gorge are 77 to 90 km^3/Ma (section S7). This missing volume represents total magmatic topographic construction, at least 270 km^3 or ~6 to 9 km^3/Ma per kilometer based on ~10- to 15-km north-south extent of the Gorge. This roughly matches inferred deep magmatic influx rates.

Last, transcrustal evidence ranging from geomorphology of river channels to seismic tomography of the crust suggests persistent, long-lived magmatism that is not directly associated with any major stratovolcano. Seismic and geodetic data show that arc magma reservoirs are commonly offset from their associated volcanoes (*49*), suggesting that sustained magma storage between adjacent volcanoes (as inferred here) is more common than previously recognized (*46*). In general, this implies that arc magma transport networks are not always strongly aligned with volcanic edifices. Our work suggests that intrusive magmatism has a broad organizing influence (*50*) spanning surface topographic development, crustal stress state, and magma ascent pathways.

MATERIALS AND METHODS

We synthesize existing structural, geophysical, and topographic data to build a case for sustained magmatic uplift in the Columbia Gorge. Data that inform the current state of the crust (gravity, heat flow, and seismic tomography) implicate magma at depth. Data that inform Pliocene/Quaternary crustal deformation include deformed hyaloclastites, arc marginal faulting, the distribution of volcanic vents around the arc front, and knickpoints in fluvial tributaries to the Columbia. Our hypothesis that ongoing long-lived magmatism is responsible for arc-centered uplift over the last ~3.5 Ma is supported by models constrained by both current and geologic data. Further information regarding our modelling approach can be found in the Supplementary Materials.

Coupled flexural uplift/transient fluvial knickpoint model

Structural deformation is inferred by compiling elevations of BV paleochannel deposits (*51*). An upper bound on the timing of deformation (3.5 Ma) is ascribed on the basis of radiometric dating of overlying basalt flows (section S1).

We model this deformation as flexure of a homogeneous thin elastic plate subject to basal pressure from magmatic intrusion. Given the lack of east-west tectonic motions resolvable in interseismic Global Navigation Satellite System (GNSS) (*52*) and paleomagnetic (*10*) data, we assume no lateral forcing on the plate in which case the thin-plate flexure equation can be written in one dimension as

$$D\frac{d^4w(y)}{dy^4} + \rho_l w(y) g = q(y) \quad (1)$$

where $w(y)$ is vertical displacement as a function of position across the arc(y), D is flexural rigidity of the plate, ρ_l is the density of material infilling the deflection (presumably magma), g is gravitational acceleration, and $q(y)$ is the vertical load on the plate. Equation 1 is solved using Fourier transforms giving

$$W(s) = \frac{Q(s)}{(2\pi s)^4 D + \rho_l g} \quad (2)$$

where $W(s)$ and $Q(s)$ are Fourier domain elevation and pressure, respectively, as a function of across-arc wave number (s). Taking an inverse Fourier transform of Eq. 2 gives the deformation of the plate in the spatial domain. From Eq. 2, an isostatic response function describes the wave number response of the crust to vertical loading of the base (fig. S9). For plausible values of Young's modulus (E), Poisson's ratio (ν), and effective elastic thickness (T_e), the observed wavelength of hyaloclastite deformation is best explained as flexural (section S6).

In the flexural regime, deformation is constrained to a characteristic wavelength (*15*) regardless of the shape of an applied load. We therefore assume a Gaussian force distribution $q(y)$ of fixed width and only vary the total force on the base of the plate in our model inversions (section S5 and fig. S7). A lack of major displacements along faults within the main region of deformation suggests mechanical continuity of the upper crust, supporting our idealization of deformation with a thin-plate model. As noted in Discussion (Fig. 3), the across-arc distribution of mapped faults, as well as the distribution of volcanic vents, is also consistent with stress patterns expected from thin-plate flexure.

Slope-break fluvial knickpoints are extracted from 1-m lidar data available through the Oregon Department of Geology and Mineral Industries (https://gis.dogami.oregon.gov/maps/lidarviewer/). Fluvial channels and catchments are extracted from raw topographic data in MATLAB (*53*).

We assume a stream power–type erosion law in which changes in elevation (z) within fluvial channels are described by

$$\frac{dz(x)}{dt} = U(x) - K\frac{\partial z(x)}{\partial x}^n A(x)^m \quad (3)$$

where x is distance upstream (and approximately orthogonal to the Columbia in most drainages), $U(x)$ is uplift rate, and $A(x)$ is drainage area upstream of a point in the channel. Empirical constants K, n, and m account for variation in erosional efficiency due to lithology, climate, and hydrology (*32*). Knickpoint locations are identified by finding the best fitting piece-wise linear fit to plots of river elevation versus drainage area-normalized distance from the channel confluence with the Columbia [$\chi(x) = \int_{x_o}^{x} \frac{A_o^\theta}{A(x)^\theta} dx$].

Below knickpoints, channel segments connected to base level through a consistent slope-area scaling relationship are assumed to represent dynamic equilibrium between uplift and erosion. The position of a knickpoint $\chi(x)_i$ in tributary channel i at across-arc position y_i in terms area-normalized upstream distance [$\chi(x)$] can be related to total uplift since the onset of the knickpoint via

$$\chi(x)_i = w(y_i)/k_s \quad (4)$$

where $w(y_i)$ is the total uplift since onset (taken to be hyaloclastite elevation at the cross arc position of the channel) and k_s is the slope of the river longitudinal profile in the χ-space (sections S2 and S3).

We perform a grid search using Eqs. 2 and 4 for 16 Columbia tributaries, over plausible values of flexural rigidity (5×10^{20} Nm $\leq D \leq 12 \times 10^{20}$ Nm), total force on the plate (31×10^6N $\leq F_{net} \leq 38 \times 10^6$ N), and the fluvial proportionality constant that maps uplift onto knickpoint positions ($110 \leq k_s \leq 170$). This we pose as a Bayesian inverse problem, in which the posterior probability density function $\sigma(m)$ is proportional to the product of assumed prior knowledge $\alpha(m)$ and a likelihood function that measures model-data misfit $L(m)$

$$\sigma(m) \propto \alpha(m)L(m) \quad (5)$$

Marginal posterior probability density functions for model parameters can be seen in fig. S7.

Supporting geophysical datasets

Heat flow (*22*) and Bouguer gravity (*21*) anomalies are detrended to highlight structure at length scales comparable to that of observed hyaloclastite uplift (110 to 130 km). A region of interest is defined with a north-south extent of 45.5°N to 45.8°N and an east-west extent of 123°W to 120.5°W (fig. S5). Ranges of detrended values for each dataset are shown in Fig. 2B. Arguments for attributing each of the respective anomalies with magma storage in the mid crust consistent with our magmatic uplift hypothesis can be found in the Supplementary Materials (sections S4, S8, and S9). In particular, the admittance between Bouguer gravity and hyaloclastite deformation suggests a flexural response to buried loading (fig. S6).

The seismic tomography model used in this study is described in detail in (*23*). To derive the relationship between V_S (shear-wave velocity) and melt fraction, we approximate the mid-lower crustal magmatic system as a complex of crystals and melt and apply an effective medium theory (*54*) to estimate its elastic properties, including compressional wave speed (V_p), shear-wave speed (V_s), and density (ρ) (*55*). We then use the estimated elastic properties of the solid and melt phase to compute the velocity of a two-phase aggregate by initially assuming air-filled pore spaces and then correcting the velocity to accommodate the liquid phase (*56*). These calculations yield melt fraction estimates of 3 to 6% for basaltic compositions and 1.5 to 4% for dacitic compositions with an estimated total melt volume of 1 to 3.7 km^3 per north-south kilometer of arc. To test plausibility of this result, we use a simple conduction model to show that the magnitude of peak heat flow measured along the arc axis is consistent with long-lived magma flux into the lower/mid crust at depths spanning observed low seismic V_S velocities (section S9).

Supplementary Materials

This PDF file includes:

Sections S1 to S9
Figs. S1 to S14
Tables S1 to S3
References

REFERENCES AND NOTES

1. C. T. A. Lee, S. Thurner, S. Paterson, W. Cao, The rise and fall of continental arcs: Interplays between magmatism, uplift, weathering, and climate. *Earth Planet. Sci. Lett.* **425**, 105–119 (2015).
2. K. M. Gregory-Wodzicki, Uplift history of the Central and Northern Andes: A review. *Bull. Geol. Soc. Am.* **112**, 1091–1105 (2000).
3. R. T. Boyd, K. M. Ames, T. A. *Johnson, Chinookan Peoples of the Lower Columbia* (University of Washington Press, ed. 1, 2013).
4. J. E. O'Connor, The evolving landscape of the Columbia river gorge: Lewis and Clark and cataclysms on the Columbia. *Oreg. Hist. Q.* **105**, 390–421 (2004).
5. J. H. Bretz, The Satsop formation of Oregon and Washington. *J. Geol.* **25**, 446–458 (1917).
6. J. E. O'Connor, S. F. Burns, Cataclysms and controversy–Aspects of the geomorphology of the Columbia River Gorge. GSA Field Guide (2009).
7. S. P. Reidel, V. E. Camp, T. L. Tolan, J. D. Kauffman, D. L. Garwood, Tectonic evolution of the Columbia River flood basalt province. *Geol. Soc Am. Spec. Paper* **497**, 293–324 (2013).
8. J. E. O'Connor, R. E. Wells, S. E. K. Bennett, C. M. Cannon, L. M. Staisch, J. L. Anderson, A. F. Pivarunas, G. W. Gordon, R. J. Blakely, M. E. Stelten, R. C. Evarts, Arc versus river—The geology of the Columbia River Gorge. *GSA Field Guide* **62**, 131–186 (2021).
9. M. H. Beeson, T. L. Tolan, The Columbia River Basalt Group in the Cascade Range: A middle miocene reference datum for structural analysis. *J. Geophys. Res.* **95**, 19547–19559 (1990).
10. R. E. Wells, R. McCaffrey, Steady rotation of the Cascade arc. *Geology* **41**, 1027–1030 (2013).
11. R. E. Wells, C. S. Weaver, R. J. Blakely, Fore-arc migration in Cascadia and its neotectonic significance. *Geology* **26**, 759–762 (1998).
12. R. M. Conrey, E. M. Taylor, J. M. Donnelly-Nolan, D. R. Sherrod, "North-Central Oregon Cascades: Exploring petrologic and tectonic intimacy in a propagating intra-arc rift" (Oregon Department of Geology and Mineral Industries, Special Paper 36, 2002), pp. 47–90.
13. E. B. Burov, M. Diament, The effective elastic thickness T_e of continental lithosphere: What does it really mean? *J. Geophys. Res.* **100**, 3905–3927 (1995).
14. P. Audet, A. M. Jellinek, H. Uno, Mechanical controls on the deformation of continents at convergent margins. *Earth Planet. Sci. Lett.* **264**, 151–166 (2007).
15. A. B. Watts, *Isostasy and Flexure of the Lithosphere* (Cambridge Univ. Press, 2001).
16. R. S. J. Sparks, K. V. Cashman, Dynamic magma systems: Implications for forecasting volcanic activity. *Elements* **13**, 35–40 (2017).
17. L. Karlstrom, S. R. Paterson, A. M. Jellinek, A reverse energy cascade for crustal magma transport. *Nat. Geosci.* **10**, 604–608 (2017).
18. D. O'Hara, N. Klema, L. Karlstrom, Development of magmatic topography through repeated stochastic intrusions. *J. Volcanol. Geotherm. Res.* **419**, 107371 (2021).
19. A. M. Wilson, J. K. Russell, Glacial pumping of a magma-charged lithosphere: A model for glaciovolcanic causality in magmatic arcs. *Earth Planet. Sci. Lett.* **548**, 116500 (2020).
20. P. Molnar, P. England, Late Cenozoic uplift of mountain ranges and global climate change: Chicken or egg? *Nature* **346**, 29–34 (1990).
21. S. Bonvalot, G. Balmino, A. Brias, M. Kuhn, A. Peyrefitte, N. Vales, R. Biancale, G. Gabalda, G. Moreaux, F. Reinquin, M. Sarrailh, "World Gravity Map: A set of global complete spherical Bouguer and isostatic anomaly maps and grids" (Technical Report, EGU General Assembly, 2012).
22. S. E. Ingebritsen, R. H. Mariner, Hydrothermal heat discharge in the Cascade Range, northwestern United States. *J. Volcanol. Geotherm. Res.* **196**, 208–218 (2010).
23. C. Jiang, B. Schmandt, G. A. Abers, E. Kiser, S. Miller, Segmentation and radial anisotropy of the deep crustal magmatic system beneath the Cascades arc. *Geochem. Geophys. Geosyst.* **24**, e2022GC010738 (2023).
24. D. O'Hara, L. Karlstrom, D. W. Ramsey, Time-evolving surface and subsurface signatures of Quaternary volcanism in the Cascades arc. *Geology* **48**, 1088–1093 (2020).
25. S. M. White, J. A. Crisp, F. J. Spera, Long-term volumetric eruption rates and magma budgets. *Geochem. Geophys. Geosyst.* **7**, 10.1029/2005GC001002, (2006).
26. S. E. Ingebritsen, R. H. Mariner, D. R. Sherrod, "Hydrothermal systems of the Cascade Range, North-Central Oregon" (U.S. Geological Survey Professional Paper 1044-L, 1994).
27. D. R. Sherrod, J. G. Smith, Geologic map of upper eocene to holocene volcanic and related rocks of the Cascade Range. *Ground Water* 10.3133/i2569, (2000).

28. Y. Takei, Effect of pore geometry on V_P/V_S: From equilibrium geometry to crack. *J. Geophys. Res. Solid Earth* **107**, ECV 6-1–ECV 6-12 (2002).
29. M. Wanke, M. A. Clynne, A. von Quadt, T. W. Vennemann, O. Bachmann, Geochemical and petrological diversity of mafic magmas from Mount St. Helens. *Contrib. to Mineral. Petrol.* **174**, 10 (2019).
30. J. R. Bulau, H. S. Waff, J. A. Tyburczy, Mechanical and thermodynamic constraints on fluid distribution in partial melts. *J. Geophys. Res. Solid Earth* **84**, 6102–6108 (1979).
31. S. D. Willett, M. T. Brandon, On steady states in mountain belts. *Geology* **30**, 175–178 (2002).
32. K. X. Whipple, R. A. DiBiase, B. T. Crosby, Bedrock Rivers. *Treatise on Geomorphology* **9**, 550–573 (2013).
33. T. C. Pierson, R. C. Evarts, J. A. Bard, "Landslides in the western Columbia Gorge, Skamania County, Washington" (U.S. Geological Survey, Scientific Investigations Map 3558, 2016).
34. B. T. Crosby, K. X. Whipple, Knickpoint initiation and distribution within fluvial networks: 236 waterfalls in the Waipaoa River, North Island, New Zealand. *Geomorphology* **82**, 16–38 (2006).
35. L. Royden, J. Taylor Perron, Solutions of the stream power equation and application to the evolution of river longitudinal profiles. *J. Geophys. Res. Earth* **118**, 497–518 (2013).
36. E. Kirby, K. X. Whipple, Expression of active tectonics in erosional landscapes. *J. Struct. Geol.* **44**, 54–75 (2012).
37. G. E. Hilley, S. Porder, F. Aron, C. W. Baden, S. A. Johnstone, F. Liu, R. Sare, A. Steelquist, H. H. Young, Earth's topographic relief potentially limited by an upper bound on channel steepness. *Nat. Geosci.* **12**, 828–832 (2019).
38. M. M. Berlin, R. S. Anderson, Modeling of knickpoint retreat on the Roan Plateau, western Colorado. *J. Geophys. Res. Earth* **112**, 10.1029/2006JF000553, (2007).
39. L. S. H. Lai, J. J. Roering, N. J. Finnegan, R. J. Dorsey, J. Y. Yen, Coarse sediment supply sets the slope of bedrock channels in rapidly uplifting terrain: Field and topographic evidence from eastern Taiwan. *Earth Surf. Process. Landf.* **46**, 2671–2689 (2021).
40. D. Lague, The stream power river incision model: Evidence, theory and beyond. *Earth Surf. Process. Landf.* **39**, 38–61 (2014).
41. A. Jefferson, G. E. Grant, S. L. Lewis, S. T. Lancaster, Coevolution of hydrology and topography on a basalt landscape in the Oregon Cascade Range, USA. *Earth Surf. Process. Landf.* **35**, 803–816 (2010).
42. C. F. Hieronymus, D. Bercovici, A theoretical model of hotspot volcanism: Control on volcanic spacing and patterns via magma dynamics and lithospheric stresses. *J. Geophys. Res.* **106**, 683–702 (2001).
43. R. Wells, R. Haugerud, A. Niem, W. Niem, L. Ma, R. Evarts, J. O'Connor, I. Madin, D. Sherrod, M. Beeson, T. Tolan, K. Wheeler, W. Hanson, M. Sawlan, "Geologic map of the greater Portland metropolitan area and surrounding region, Oregon and Washington" (U.S. Geological Survey, Scientific Investigations Map 3443, 2020).
44. D. Garcia-Castellanos, Interplay between lithospheric flexure and river transport in foreland basins. *Basin Res.* **14**, 89–104 (2002).
45. W. Hildreth, "Quaternary magmatism in the Cascades–Geologic perspectives" (USGS Professional Paper, 2007).
46. P. A. Bedrosian, J. R. Peacock, E. Bowles-Martinez, A. Schultz, G. J. Hill, Crustal inheritance and a top-down control on arc magmatism at Mount St Helens. *Nat. Geosci.* **11**, 865–870 (2018).
47. J. R. Muller, G. Ito, S. J. Martel, Effects of volcano loading on dike propagation in an elastic half-space. *J. Geophys. Res.* **106**, 11101–11113 (2001).
48. E. S. Garcia, D. T. Sandwell, K. M. Luttrell, An iterative spectral solution method for thin elastic plate flexure with variable rigidity. *Geophys. J. Int.* **200**, 1012–1028 (2015).
49. A. H. Lerner, D. O'Hara, L. Karlstrom, S. K. Ebmeier, K. R. Anderson, S. Hurwitz, The prevalence and significance of offset magma reservoirs at arc volcanoes. *Geophys. Res. Lett.* **47**, e2020GL087856 (2020).
50. L. Karlstrom, J. Dufek, M. Manga, Organization of volcanic plumbing through magmatic lensing by magma chambers and volcanic loads. *J. Geophys. Res. Solid Earth* **114**, 10.1029/2009JB006339, (2009).
51. C. M. Cannon, R. Evarts, "Extent of Pliocene hyaloclastic deposits and related lava flows in the Columbia Gorge, Oregon and Washington" (U.S. Geological Survey, Data Release, 2023).
52. R. McCaffrey, R. W. King, S. J. Payne, M. Lancaster, Active tectonics of northwestern U.S. inferred from GPS-derived surface velocities. *J. Geophys. Res. Solid Earth* **118**, 709–723 (2013).
53. W. Schwanghart, D. Scherler, Short Communication: TopoToolbox 2 - MATLAB-based software for topographic analysis and modeling in Earth surface sciences. *Earth Surf. Dyn.* **2**, 1–7 (2014).
54. J. G. Berryman, Long-wavelength propagation in composite elastic media ii. ellipsoidal inclusions. *J. Acoust. Soc. Am.* **68**, 1820–1831 (1980).
55. R. Maguire, B. Schmandt, J. Li, C. Jiang, G. Li, J. Wilgus, M. Chen, Magma accumulation at depths of prior rhyolite storage beneath yellowstone caldera. *Science* **378**, 1001–1004 (2022).
56. F. Gassmann, Elastic waves through a packing of spheres. *Geophysics* **16**, 673–685 (1951).
57. J. D. Mcclaughry, T. J. Wiley, R. M. Conrey, C. B. Jones, K. E. Lite, "Digital geologic map of the Hood River Valley, Hood River and Wasco counties, Oregon" (State of OregonOregon Department of Geology and Mineral Industries, Technical Report, 2012).
58. Pacific Northwest Seismic Network (2023).
59. M. A. Korosec, "Geologic map of the Hood River quadrangle, Washington and Oregon" (U. S. Department of Energy Office of Scientific and Technical Information, Technical Report, 1987).
60. S. P. Reidel, T. L. Tolan, The Grande Ronde Basalt, Columbia River Basalt Group. *Geol. Soc. Am. Spec. Paper* **497**, 10.1130/2013.2497(05), (2013).
61. S. P. Reidel, T. L. Tolan, The late Cenozoic evolution of the Columbia River system in the Columbia River flood basalt province. *Geol. Soc Am. Spec. Paper* **497**, 10.1130/2013.2497 (08), (2013).
62. T. L. Tolan, M. H. Beeson, Intracanyon flows of the Columbia River Basalt Group in the lower Columbia River Gorge and their relationship to the troutdale formation. *Bull. Geol. Soc. Am.* **95**, 463–477 (1984).
63. R. M. Conrey, D. R. Sherrod, K. Uto, S. Uchiumi, potassium-argon ages from mount hood area of Cascade Range, Northern Oregon. *Isochron/West* **63**, 10–20 (1996).
64. R. D. Swanson, "A stratigraphic-geochemical study of the Troutdale Formation and Sandy River Mudstone in the Portland Basin and lower Columbia River Gorge," thesis, Portland State University, Portland, OR (1986).
65. R. J. Fleck, J. T. Hagstrum, A. T. Calvert, R. C. Evarts, R. M. Conrey, $^{40}Ar/^{39}Ar$ geochronology, paleomagnetism, and evolution of the boring volcanic field, Oregon and Washington, USA. *Geosphere* **10**, 1283–1314 (2014).
66. R. Conrey, D. R. Sherrod, P. R. Hooper, D. A. Swanson, Diverse primitive magmas in the Cascade arc, Northern Oregon and Southern Washington. *Can. Mineral.* **35**, 367–396 (1997).
67. J. T. Hagstrum, R. J. Fleck, R. C. Evarts, A. T. Calvert, Paleomagnetism and $^{40}Ar/^{39}Ar$ geochronology of the Plio-Pleistocene Boring Volcanic Field: Implications for the geomagnetic polarity time scale and paleosecular variation. *Phys. Earth Planet. In.* **262**, 101–115 (2017).
68. R. Conrey, K. Uto, S. Uchiami, M. Beeson, I. Madin, T. Tolan, D. A. Swanson, Potassium-argon ages of Boring Lava, northwest Oregon and southwest Washington. *Isochron/West* **63**, 3–9 (1996).
69. J. L. Anderson, "Structural geology and ages of deformation of a portion of the southwest Columbia Plateau," thesis, Los Angeles, University of Southern California, Los Angeles, CA (1987).
70. J. J. Flint, Stream gradient as a function of order, magnitude, and discharge. *Water Resour. Res.* **10**, 969–973 (1974).
71. J. T. Hack, F. A. Seaton, T. B. Nolan, in *Studies of Longitudinal Stream Profiles in Virginia and Maryland* (U.S. Government Printing Office, 1957), pp. 45–97.
72. D. R. Montgomery, W. E. Dietrich, Channel initiation and the problem of landscape scale. *Science* **255**, 826–830 (1992).
73. J. T. Perron, L. Royden, An integral approach to bedrock river profile analysis. *Earth Surf. Process. Landf.* **38**, 570–576 (2013).
74. K. X. Whipple, Bedrock rivers and the geomorphology of active orogens. *Annu. Rev. Earth Planet. Sci.* **32**, 151–185 (2004).
75. J. G. Venditti, T. Li, E. Deal, E. Dingle, M. Church, Struggles with stream power: Connecting theory across scales. *Geomorphology*, 106817 (2020).
76. L. Goren, M. Fox, S. D. Willett, Tectonics from fluvial topography using formal linear inversion: Theory and applications to the Inyo Mountains, California. *J. Geophys. Res. Earth Surf.* **119**, 1651–1681 (2014).
77. B. A. Adams, K. X. Whipple, A. M. Forte, A. M. Heimsath, K. V. Hodges, Climate controls on erosion in tectonically active landscapes. *Sci. Adv.* **6**, eaaz3166 (2020).
78. S. F. Gallen, D. Fernández-Blanco, A new data-driven Bayesian inversion of fluvial topography clarifies the tectonic history of the Corinth Rift and reveals a channel steepness threshold. *J. Geophys. Res. Earth* **126**, e2020JF005651 (2021).
79. C. Wobus, K. X. Whipple, E. Kirby, N. Snyder, J. Johnson, K. Spyropolou, B. Crosby, D. Sheehan, Tectonics from topography: Procedures, promise, and pitfalls. *Geol. Soc Am. Spec. Paper* **398**, 10.1130/2006.2398(04), (2006).
80. D. R. Montgomery, E. Foufoula-Georgiou, Channel network source representation using digital elevation models. *Water Resour. Res.* **29**, 3925–3934 (1993).
81. D. L. Turcotte, G. Schubert, *Geodynamics* (Cambridge Univ. Press, ed. 3, 2014).
82. J. P. Perkins, K. M. Ward, S. L. De Silva, G. Zandt, S. L. Beck, N. J. Finnegan, Surface uplift in the Central Andes driven by growth of the Altiplano Puna Magma Body. *Nat. Commun.* **7**, 13185 (2016).

83. J. R. Delph, A. M. Thomas, A. Levander, Subcretionary tectonics: Linking variability in the expression of subduction along the Cascadia forearc. *Earth Planet. Sci. Lett.* **556**, 116724 (2021).
84. D. W. Forsyth, Subsurface loading and estimates of the flexural rigidity of continental lithosphere. *J. Geophys. Res.* **90**, 12623–12632 (1985).
85. R. J. Blakely, Extent of partial melting beneath the Cascade Range, Oregon: Constraints from gravity anomalies and ideal-body theory. *J. Geophys. Res.* **99**, 2757–2773 (1994).
86. C. F. Williams, J. DeAngelo, Mapping geothermal potential in the Western United States. *Geothermal Resources Council Transactions* **32**, 155–161 (2008).
87. D. T. Sandwell, Thermomechanical evolution of oceanic fracture zones. *J. Geophys. Res.* **89**, 11401–11413 (1984).
88. K. Mosegaard, A. Tarantola, Monte Carlo sampling of solutions to inverse problems. *J. Geophys. Res.* **100**, 12431–12447 (1995).
89. A. Tarantola, *Inverse Problem Theory and Methods for Model Parameter Estimation* (Society for Industrial and Applied Mathematics, 2005).
90. R. Walcott, Flexural rigidity, thickness, and viscosity of the lithosphere. *J. Geophys. Res.* **75**, 3941–3954 (1970).
91. J. A. D. Connolly, The geodynamic equation of state: What and how. *Geochem. Geophys. Geosyst.* **10**, 10.1029/2009GC002540, (2009).
92. M. Wanke, O. Karakas, O. Bachmann, The genesis of arc dacites: The case of Mount St. Helens, WA. *Contrib. Mineral. Petrol.* **174**, 7 (2019).
93. D. L. Blatter, T. W. Sisson, W. B. Hankins, Voluminous arc dacites as amphibole reaction-boundary liquids. *Contrib. Mineral. Petrol.* **172**, 27 (2017).
94. W. P. Leeman, J. F. Lewis, R. C. Evarts, R. M. Conrey, M. J. Streck, Petrologic constraints on the thermal structure of the cascades arc. *J. Volcanol. Geotherm. Res.* **140**, 67–105 (2005).
95. K. Ueki, H. Iwamori, Density and seismic velocity of hydrous melts under crustal and upper mantle conditions. *Geochem. Geophys. Geosyst.* **17**, 1799–1814 (2016).
96. M. Paulatto, E. E. Hooft, K. Chrapkiewicz, B. Heath, D. R. Toomey, J. V. Morgan, Advances in seismic imaging of magma and crystal mush. *Front. Earth Sci.* **10**, 970131 (2022).
97. M. Holness, Melt–solid dihedral angles of common minerals in natural rocks. *J. Petrol.* **47**, 791–800 (2006).
98. M. O. Saar, M. Manga, Depth dependence of permeability in the Oregon Cascades inferred from hydrogeologic, thermal, seismic, and magmatic modeling constraints. *J. Geophys. Res. Solid Earth* **109**, 10.1029/2003JB002855, (2004).
99. S. E. Ingebritsen, D. R. Sherrod, R. H. Mariner, Heat flow and hydrothermal circulation in the cascade range, north-central Oregon. *Science* **243**, 1458–1462 (1989).
100. D. D. Blackwell, J. L. Steele, S. Kelley, M. A. Korosec, Heat flow in the State of Washington and thermal conditions in the Cascade Range. *J. Geophys. Res.* **95**, 19495–19516 (1990).
101. C. B. Till, A. J. Kent, G. A. Abers, H. A. Janiszewski, J. B. Gaherty, B. W. Pitcher, The causes of spatiotemporal variations in erupted fluxes and compositions along a volcanic arc. *Nat. Commun.* **10**, 1350 (2019).

Acknowledgments: This work benefited greatly from discussions with J. Roering, K. Cashman, R. Conrey, T. Tolan, and L. S.-H. Lai. We thank R. Denlinger for constructive comments that improved the manuscript. Any use of trade, firm, or product names is for descriptive purposes only and does not imply endorsement by the US government. **Funding:** This work was supported by NSF CAREER 1848554 (L.K.) and Australian Research Council Discovery Early Career Researcher Award DE220100907 (C.J). **Author contributions:** Conceptualization: N.K., L. K., C.C., J.O., and B.S. Methodology: N.K., L.K., C.J., and B.S. Data curation: C.C., L.K., R.W., and C.J. Investigation: N.K., J.O., and C.C. Visualization: N.K., C.J., and J.O. Supervision: N.K., L.K., and J.O. Writing—original draft: N.K., L.K., C.J., C.C., and J.O. Writing—review and editing: N.K., L.K., J.O., R.W., and B.S. **Competing interests:** The authors declare that they have no competing interests. **Data and materials availability:** All data needed to evaluate the conclusions in the paper are present in the paper and/or the Supplementary Materials. The lidar data are available for download at https://gis.dogami.oregon.gov/maps/lidarviewer/. Topotoolbox is a topographic analysis toolkit for MATLAB available at https://topotoolbox.wordpress.com/download/. The open source package ElasticC is available at http://github.com/michpaulatto/ElasticC. Geophysical and structural datasets can be accessed through the references in the paper.

Submitted 20 June 2023
Accepted 20 November 2023
Published 20 December 2023
10.1126/sciadv.adj3357